



Published in final edited form as:

*Magn Reson Med.* 2009 May ; 61(5): 1242–1248. doi:10.1002/mrm.21901.

## Optimal $k$ -Space Sampling for Dynamic Contrast-Enhanced MRI with an Application to MR Renography

Ting Song<sup>1,2,\*</sup>, Andrew F. Laine<sup>2</sup>, Qun Chen<sup>1</sup>, Henry Rusinek<sup>1</sup>, Louisa Bokacheva<sup>1</sup>, Ruth P. Lim<sup>1</sup>, Gerhard Laub<sup>3</sup>, Randall Kroeker<sup>4</sup>, and Vivian S. Lee<sup>1</sup>

<sup>1</sup>Department of Radiology, New York University School of Medicine, New York, New York.

<sup>2</sup>Department of Biomedical Engineering, Columbia University, New York, New York.

<sup>3</sup>Siemens Medical Solutions, Los Angeles, California.

<sup>4</sup>Siemens Medical Solutions, Winnipeg, MB, Canada.

### Abstract

For time-resolved acquisitions with  $k$ -space undersampling, a simulation method was developed for selecting imaging parameters based on minimization of errors in signal intensity versus time and physiologic parameters derived from tracer kinetic analysis. Optimization was performed for time-resolved angiography with stochastic trajectories (TWIST) algorithm applied to contrast-enhanced MR renography. A realistic 4D phantom comprised of aorta and two kidneys, one healthy and one diseased, was created with ideal tissue time-enhancement pattern generated using a three-compartment model with fixed parameters, including glomerular filtration rate (GFR) and renal plasma flow (RPF). TWIST acquisitions with different combinations of sampled central and peripheral  $k$ -space portions were applied to this phantom. Acquisition performance was assessed by the difference between simulated signal intensity (SI) and calculated GFR and RPF and their ideal values. Sampling of the 20% of the center and 1/5 of the periphery of  $k$ -space in phase-encoding plane and data-sharing of the remaining 4/5 minimized the errors in SI (<5%), RPF, and GFR (both <10% for both healthy and diseased kidneys). High-quality dynamic human images were acquired with optimal TWIST parameters and 2.4 sec temporal resolution. The proposed method can be generalized to other dynamic contrast-enhanced MRI applications, e.g., MR angiography or cancer imaging.

### Keywords

time-resolved MRI; dynamic contrast-enhanced MRI; MR renography; optimal sampling; TWIST

Dynamic contrast-enhanced MR imaging (DCE MRI) plays an important role in many applications, such as perfusion imaging in oncology (1), MR angiography (2), and MR renography (MRR) (3,4). Among the key requirements of DCE MRI is achieving sufficiently high temporal resolution without sacrificing spatial resolution and anatomic coverage. Strategies for achieving both high temporal and spatial resolution often employ  $k$ -space undersampling, such as keyhole imaging (5), blocked regional interpolation scheme for  $k$ -space (BRISK) (6), continuous update with random encoding (CURE) (7), time-resolved imaging of contrast kinetics (TRICKS) (8,9), and k-t Broad-use Linear Acquisition Speed-up Technique

(k-t BLAST) (10). The resulting image artifacts and spatial resolution depend on the size of the frequently updated portion of  $k$ -space (the “center”) and on the nature and extent of undersampling of the periphery. A large central portion of  $k$ -space is likely to produce high-quality images but lower temporal resolution. On the other hand, undersampling of the peripheral  $k$ -space regions can result in ringing artifacts, which not only impair postprocessing steps, such as image segmentation, but may also obscure visualization and characterization of smaller structures. Furthermore, undersampling may distort enhancement curves, especially when the signal is changing rapidly, for example, during first-pass perfusion, and can affect the accuracy of kinetic modeling parameters.

Despite increasing use of fast acquisition techniques and DCE MRI in diagnostic radiology, few studies have explored the problem of balancing the temporal and spatial properties of the acquisition protocol. A number of studies have evaluated the minimum temporal resolution required for accurate derivation of parameters using tracer kinetic modeling from dynamic data (11); however, there is no general methodology to guide the selection of optimal imaging parameters necessary to achieve proper temporal resolution as well as good-quality images. In humans, the main obstacle to optimizing the parameters for DCE MRI is the difficulty of performing repeated measurements in the same subject and the large variability of physiologic conditions across subjects. Constructing a physical phantom that can adequately represent a realistic contrast enhancement is also very difficult. Thus, one alternative is to create optimization routines that rely on simulated objects with properties resembling *in vivo* tissues.

We propose such a routine for determining the optimal  $k$ -space sampling parameters for DCE MRI based on minimization of errors in signal intensity (SI) curves and the physiologic measures derived from tracer kinetic analysis. We apply our method to the renal functional MR examination, or MR renography (MRR), which monitors the passage of an intravenously injected contrast agent, typically a gadolinium chelate, through the abdominal aorta and the kidneys and enables measuring such clinically important renal functional parameters as the glomerular filtration rate (GFR) and renal plasma flow (RPF) (12). Our optimization procedure emulates the acquisition of undersampled images of a simulated, four-dimensional (4D, three spatial dimensions and one temporal) phantom that consists of the abdominal aorta and kidneys. We hypothesize that such a phantom adequately represents contrast enhancement observed in a real MRR examination, and simulated imaging of this phantom with an accelerated acquisition technique enables selecting optimal acquisition parameters that can be subsequently applied to *in vivo* studies. We implement our method using a new  $k$ -space undersampling and data-sharing method known as Time-resolved angiography With Stochastic Trajectories (TWIST) (13,14).

## MATERIALS AND METHODS

### TWIST Overview

Consider a 3D Cartesian  $k$ -space with readout direction  $K_x$  and phase-encoding (PE) directions  $K_y$  and  $K_z$ . The TWIST sampling scheme is applied in the PE plane  $K_y - K_z$  as follows. First, all points in PE plane (each point corresponding to one readout line) with coordinates  $(k_y, k_z)$  are sorted by their polar coordinates  $(k_r, \Theta)$ , first by increasing radial distance  $k_r = \sqrt{k_y^2 + k_z^2}$  (primary sort key) and then by increasing azimuthal angle  $\Theta$  ( $0 \leq \Theta < 2\pi$ ), which is measured counterclockwise from the  $K_y$ -axis (secondary sort key). The points on the resulting sorted list are then split by a critical radial distance  $K_c$  into two subsets: a low-frequency subset A containing points with  $k_r < K_c$  and a complementary, high-frequency subset B with  $k_r \geq K_c$  (Fig. 1a). Next, every point in region B is sequentially assigned to one of  $N$  disjoint and nonoverlapping subsets (trajectories)  $B_j, j = 1, 2, \dots, N$ , of approximately equal size.

During acquisition of dynamic series, full  $k$ -space is collected only once, either for the very first image or the last. For all other images, region A is sampled fully every time, but only one B trajectory is acquired, and the missing points in B are copied from the previous image (forward data-sharing scheme) or from the subsequent image (backward sharing) (Fig. 1b). Sampling of  $k$ -space starts at the outer edge of A ( $k_r \approx K_c$ ) and proceeds toward the origin via all the odd ( $k_r, \theta$ ) points from the sorted list. Upon reaching the minimum  $k_r$ , the sampling direction is reversed and every even point is acquired until the edge of A is reached. Then in region B the trajectory  $B_j$  is sampled by first acquiring every odd point on the way toward larger  $k_r$  and then every even point on the way back toward  $K_c$  (Fig. 1c). At the next timepoint, region A is again sampled fully and only the trajectory  $B_{j+1}$  is acquired (Fig. 1d).

The degree of TWIST undersampling is described by two parameters:  $p_A$ , which specifies the proportion of the central region A, and  $p_B$ , which determines the density of sampling of region B:

$$p_A = \frac{K_c}{\max(K_y, K_z)} \quad [1]$$

$$p_B = 1/N. \quad [2]$$

For example, in Fig. 1  $p_A = 0.5$ ,  $N = 3$ , and  $p_B \approx 0.33$ .

The TWIST acquisition time  $TA_{TWIST}$  can be expressed in terms of the full  $k$ -space acquisition time  $TA_{full}$ ,  $p_B$ , the size of area A ( $S_A$ ), and the total area of PE plane ( $S_{PE}$ ):

$$TA_{TWIST} = TA_{full} \left( \frac{S_A}{S_{PE}} + \left( 1 - \frac{S_A}{S_{PE}} \right) p_B \right). \quad [3]$$

Thus, TWIST offers two independent ways to improve the temporal resolution: by reducing the size of region A (by lowering  $p_A$ ) or by sampling region B more sparsely (by lowering  $p_B$ ). Both methods have certain tradeoffs: lowering  $p_A$  will sacrifice the low spatial frequency information, while lowering  $p_B$  will decrease the fidelity of small features and fine image texture.

### Optimization of TWIST Parameters for MR Renography

We sought to define the optimal TWIST MRR parameters that balanced the competing temporal and spatial resolution needs to produce the lowest errors in acquired SI and physiological renal parameters, RPF, and GFR, relative to their predefined “real” values. Our simulation procedure for selecting the optimal parameters  $p_A$  and  $p_B$  included the following steps:

1. Concentration versus time curves for the renal cortex and renal medulla were generated using a tracer kinetic renal model (12) with a measured aortic enhancement curve serving as the input function and fixed predefined “ideal” model parameters RPF and GFR. The concentration curves were then converted into SI. In  $k$ -space raw data, 10% of pre-enhanced SI value was added to each timepoint to resemble a high-noise experimental situation (15). A 4D phantom of aorta and two kidneys was created with SI in each voxel varying according to the corresponding model-derived tissue SI versus time dependence (Fig. 2).

2. At each timepoint, the 3D phantom image (frame) was Fourier-transformed to obtain  $k$ -space data. TWIST acquisitions with different combinations of pA and pB parameters were applied to each of these  $k$ -space datasets to simulate different degrees of undersampling.
3. The undersampled  $k$ -space datasets were Fourier-transformed back into the real space to simulate image reconstruction.
4. Reconstructed images were segmented into cortex and medulla, and aortic, cortical, and medullary SI curves were derived and converted into contrast concentrations.
5. Cortical and medullary concentration versus time curves were fitted using the same renal model (with aortic curve serving as the input function) to extract GFR and RPF.
6. Simulated TWIST images and renal functional parameters derived from undersampled data were compared to the ideal reference images and initial functional parameters. Values of pA and pB which produced the smallest error in SI, RPF, and GFR relative to their ideal values were considered to be optimal.

These steps are described in detail below.

### Simulated 3D Renal Phantom

A simulated 3D phantom of the abdominal aorta, renal arteries, and two kidneys was created to represent the anatomic structures typically examined in MRR studies (Fig. 2a). Simulations were performed using MATLAB (MathWorks, Natick, MA). The right kidney was of normal size with length  $L = 11$  cm and average cortical thickness  $d = 1$  cm (whole kidney volume  $V_R = 196$  mL). The left kidney was atrophic with  $L = 9$  cm and reduced cortical thickness  $d = 0.8$  cm ( $V_L = 99$  mL). The anatomy of the intrarenal regions was constructed based on the in vivo MRR images acquired at 1.5T (Avanto; Siemens Medical Solutions, Erlangen, Germany) with a  $T_1$ -weighted 3D gradient echo sequence and segmented manually into cortex, medulla, and collecting system by an experienced radiologist (4).

### 4D Phantom Contrast Kinetics

The SI versus time behavior of aortic/arterial, cortical, and medullary regions of the phantom was simulated using a three-compartment tracer kinetic renal model, which has been shown to provide adequate fits to MRR data, reasonably accurate estimates of GFR, and good stability in the presence of noise (12) (see Appendix).

The aortic enhancement curve that serves as the arterial input function for this model was derived from MRR images of a patient with well-functioning kidneys and normal cardiac output acquired after an intravenous injection of 4 mL Gd-DTPA and 20 mL saline flush, both injected at the rate of 2 mL/sec. The aortic curve was interpolated to the temporal resolution of 0.1 sec and used to generate two sets of cortical and medullary concentration curves, one with parameters characteristic of a healthy kidney ( $RPF = 346$  mL/min,  $GFR = 77$  mL/min,  $V_{aCx} = 45.5$  mL,  $f_p = 0.4$ ,  $f_L = 0.01$ ), and the other with parameters typical for a diseased kidney ( $RPF = 78$  mL/min,  $GFR = 17$  mL/min,  $V_{aCx} = 18$  mL,  $f_p = 0.2$ ,  $f_L = 0.13$ ) (Fig. 2).

The aortic and model-derived cortical and medullary concentrations were converted into SI values (16). Every voxel of the phantom corresponding to the aorta and renal arteries was assigned the aortic SI, and each renal region of the healthy and diseased kidneys were assigned SI curves according to their function.

## TWIST Simulations

For each 3D image,  $k$ -space data were generated by Fourier transformation and sampled using the TWIST technique. Sixteen different combinations of  $p_A$  and  $p_B$  parameters were considered, with each parameter taking values 0.50, 0.33, 0.20, and 0.10. The corresponding acquisition times ranged from 6.7 sec for  $p_A = 0.5$ ,  $p_B = 0.5$  (conservative undersampling) to 1.2 sec for  $p_A = 0.1$ ,  $p_B = 0.1$  (drastic undersampling), compared to  $TA_{full} = 9$  sec. TWIST acquisition and subsequent reconstruction of each 3D image required 6 min of computing time on a 2.4 GHz 64-bit AMD server running Red Hat Linux Enterprise AS (Red Hat; Raleigh, NC).

## SI, RPF, and GFR Errors Due to TWIST Undersampling

A fixed image mask from the original phantom image was used to segment the reconstructed TWIST images into aorta, cortex, and medulla. The regional SI versus time curves were converted into gadolinium concentration (16); cortical and medullary curves were then fitted by a three-compartment renal model to derive RPF, GFR, and other parameters (12).

The performance of each ( $p_A$ ,  $p_B$ ) combination was assessed by the errors between the SI, RPF, and GFR determined from the TWIST-undersampled data relative to their ideal preset values (Fig. 2b,c). The SI error was defined as the root mean square difference between the measured and ideal SI across all  $T$  timepoints summed over  $M$  regions ( $M = 3$  for aorta, cortex, and medulla):

$$SI \text{ Error} = \frac{1}{M} \sum_{j=1}^M \sqrt{\frac{1}{T} \sum_{t=1}^T (SI_{\text{measured}}(t, j) - SI_{\text{true}}(t, j))^2}. \quad [4]$$

Absolute errors in the renal functional parameters, *RPF Error* and *GFR Error*, were defined as:

$$RPF \text{ Error} = |RPF_{\text{measured}} - RPF_{\text{true}}|, \quad [5]$$

$$GFR \text{ Error} = |GFR_{\text{measured}} - GFR_{\text{true}}|, \quad [6]$$

and the relative errors were defined as  $RPF \text{ Error}/RPF_{\text{true}}$  and  $GFR \text{ Error}/GFR_{\text{true}}$ , respectively. The errors in SI, RPF, and GFR were computed at the 16 aforementioned combinations of ( $p_A$ ,  $p_B$ ), interpolated for intermediate values, and displayed as 2D surface plots.

## In Vivo TWIST Imaging

After providing written informed consent, a 48-year-old female patient with hypertension was imaged at 1.5T (Avanto; Siemens) after an injection of 2 mL of Gd-DTPA (Magnevist; Berlex Laboratories, Wayne, NJ) and 20 mL saline flush both injected at a rate of 2 mL/min with an automated injector (Spectris; Medrad, Indianola, PA). Images were acquired during intermittent breath-holding using TWIST GRE sequence (TR/TE/FA = 2.61/1.07/12°, acquired matrix 256 × 161 × 26, FOV 425 mm × 425 mm × 100 mm, true voxel size 1.7 × 2.6 × 3.8 mm<sup>3</sup>, bandwidth 650 Hz). Acquisition time for full  $k$ -space was  $TA_{full} = 7.1$  sec and  $TA_{TWIST} = 2.4$  sec per 3D image with  $p_A = 0.2$  and  $p_B = 0.2$ .

## RESULTS

### Temporal Resolution versus Image Artifacts

Phantom images acquired with different degrees of undersampling shown in Fig. 3 illustrate the tradeoffs between the temporal resolution and image artifacts. For moderate undersampling, ( $pA = 0.5$ ,  $pB = 0.5$ ), the image is almost artifact-free, but the relatively long acquisition time (6.7 sec/frame) results in inaccurate representation of the aortic SI peak. With high undersampling, ( $pA = 0.1$ ,  $pB = 0.1$ ), the temporal resolution improves to 1.2 sec/frame and allows better tracking of the rapidly changing aortic SI at the cost of severe ringing artifacts that are mainly created by the aorta and extend over the kidneys. Note that the peak SI value remains underestimated even at the best temporal resolution because of sharing of  $k$ -space data from adjacent timepoints.

### Errors in SI, RPF and GFR

The errors in SI, RPF, and GFR for healthy and diseased kidneys are plotted in Fig. 4. For both kidneys, the average SI errors showed a minimum of less than 5% at  $pA \approx 0.20$ ,  $pB \approx 0.20$ . SI error increased sharply as both  $pA$  and  $pB$  approached 0.5.

The RPF error distribution was similar to the distribution of SI errors, with a single minimum found at  $pA \approx 0.20$  and  $pB \approx 0.20$ . The GFR errors appear to be lower and relatively insensitive to  $pA$ ,  $pB$  and are less than 10% throughout the range of TWIST parameters examined.

### In Vivo Imaging

Representative in vivo kidney images acquired with  $pA = 0.2$  and  $pB = 0.2$  are shown in Fig. 5 at  $t = 0$  sec, 19.3 sec, 24.1 sec, and 70.1 sec after the injection and demonstrate feasibility of using TWIST for MRR.

## DISCUSSION

For an accurate representation of both morphologic and kinetic kidney characteristics, the DCE MRI acquisitions must have high temporal resolution and be free of distortions and artifacts; however, these are competing demands that require a compromise. This issue has been addressed by repeated imaging of subjects and qualitative assessment of the resulting data (17–19). There are two problems with this empirical approach. First, there are typically no ground truth reference values available for evaluating the measurement results. Second, repeating experiments on the same patient in order to compare different acquisition parameters is time-consuming and often impractical because protocols require administration of contrast material.

To address such optimization issues, we developed a simulation-based method for testing dynamic acquisitions that employ  $k$ -space undersampling and sharing to improve temporal resolution. We demonstrated the validity of the proposed method using a TWIST undersampling algorithm applied to the functional renal imaging, MR renography. Our simulations established that the TWIST parameters that minimized the errors in signal intensity, RPF and GFR, are  $pA \approx 0.20$  and  $pB \approx 0.20$ , with 2-sec acquisition time per 3D volume. With these parameters, the SI errors were within 5% and the RPF error was less than 10% for both healthy and diseased kidneys. The computation of GFR was less sensitive to the acquisition protocol, with errors in GFR below 10% throughout the entire range of  $pA$  and  $pB$  values examined. Our simulations also showed that without TWIST the GFR error was about 15%, in agreement with other simulated and clinical results (12).



Although these results are specific to MRR, the proposed simulation framework is suitable for any time-resolved imaging acquisition in which changes in contrast enhancement are used to estimate functional tissue parameters, for example, perfusion imaging of cancer (17,18). The simulation parameters should be modified to reflect the scenarios relevant to a particular study: for example, in cancer perfusion, higher contrast doses injected at different rates may have to be simulated in order to determine their influence on tracer kinetic tissue parameters, such as blood flow, vascular permeability, or vascular volume.

There are several limitations of our work. First, physiological noise (due mostly to respiratory motion) was ignored. In our routine protocols, renal motion is minimized with breath-holding and postprocessing using image registration across timeframes. However, with TWIST, motion artifacts would be expected to affect multiple frames because data are shared temporally. Second, our simulation was applied to a particular set of physiologic parameters (one example of a normal and diseased kidney with one aortic input function) and imaging conditions (no parallel imaging). However, our method can be easily extended to other physiological states and acquisition protocols.

Recent publications suggest that in patients with impaired renal function gadolinium-containing contrast agents may be associated with nephrogenic systemic fibrosis (NSF). This study simulated a low-dose MRR examination in which 4 mL of Gd-DTPA, or  $\approx 0.02$  mmol/kg, was used. The safety of gadolinium contrast agents in patients with renal disease remains to be further investigated; however, the use of low contrast doses may help to minimize the risk of NSF and also avoid the signal loss due to  $T_2^*$  effects (20).

In conclusion, a simulation framework for optimizing the acceleration parameters for DCE MRI has been shown to be useful for selecting undersampling parameters of TWIST applied to MR renography. For both healthy and diseased kidneys, SI, RPF, and GFR errors were minimized at  $pA \approx 0.20$  and  $pB \approx 0.20$ . In vivo validation studies remain to be performed.

## Acknowledgments

The authors thank Dr. Jeff L. Zhang for help on renal modeling, Dr. Niels Oesingmann (Siemens Medical Solutions USA) for thoughtful discussions, and Ms. Keyma Prince for help with image analysis.

Grant sponsor: National Institute of Diabetes and Digestive and Kidney Diseases (NIDDK); Grant sponsor: National Institutes of Health (NIH); Grant numbers: R01 DK063183 and R01 DK067523.

## APPENDIX

This previously validated three-compartment renal model (12) represents the kidney as a combination of serial compartments: the arterial compartment with concentration  $A(t)$ , shared by cortex and medulla, the proximal tubules,  $P(t)$ , contained only in the cortex, and the loops of Henle,  $L(t)$ , contained only in medulla. The compartmental concentrations are derived from the mass conservation principle, and the cortical and medullary regional concentrations are expressed as combinations of  $A$ ,  $P$ , and  $L$ :

$$A(t) = \frac{\text{RPF}}{(V_{\text{aCx}} + V_{\text{aMed}})} \int_0^t A o_p(y) e^{\frac{-\text{RPF}}{(V_{\text{aCx}} + V_{\text{aMed}})}(t-y)} dy, \quad [\text{A1}]$$

$$P(t) = \frac{\text{GFR}}{V_p} \int_0^t A(y) e^{\frac{-\text{GFR}(1-f_p)}{V_p}(t-y)} dy \quad [\text{A2}]$$

$$L(t) = \frac{\text{GFR}(1 - f_p)}{V_L} \int_0^t P(y) e^{-\frac{\text{GFR}(1 - f_p - f_L)}{V_L}(t-y)} dy \quad [\text{A3}]$$

$$C_X(t) = \frac{V_{aCx}}{V_{Cx}} A(t) + \frac{V_p}{V_{Cx}} P(t), \quad [\text{A4}]$$

$$\text{Med}(t) = \frac{V_{aMed}}{V_{Med}} A(t) + \frac{V_L}{V_{Med}} L(t). \quad [\text{A5}]$$

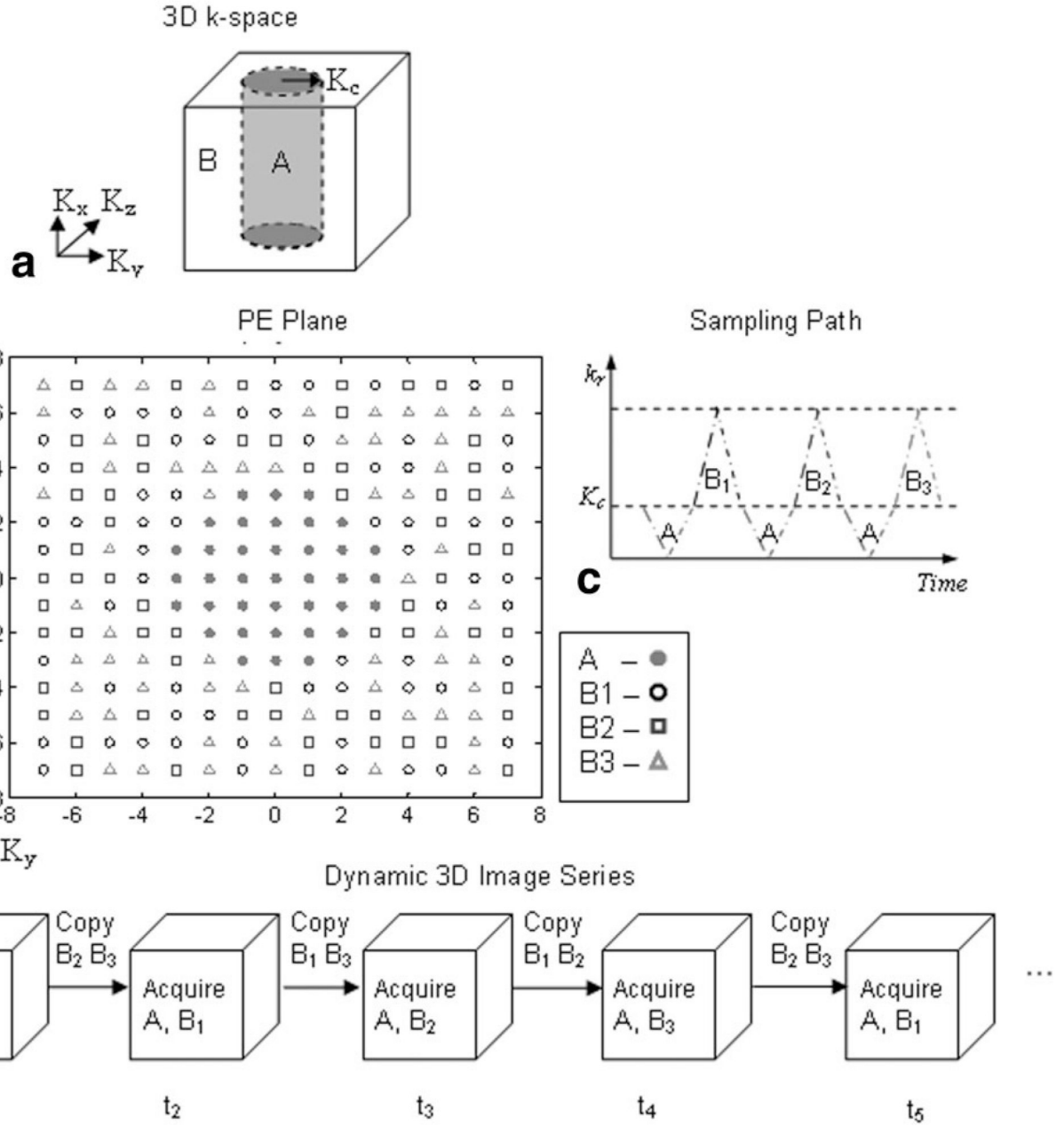
Here the aortic plasma enhancement  $A_o(t)$  is the input function,  $V_{Cx}$  and  $V_{Med}$  are volumes,  $V_{aCx}$  and  $V_{aMed}$  are the cortical and medullary vascular volumes,  $V_p$  and  $V_L$  are the volumes of P and L (fixed at  $0.3V_{Cx}$  and  $0.5V_{Med}$ , respectively), and  $f_p$  and  $f_L$  are fractions of contrast-free filtrate flow reabsorbed in P and L.

## REFERENCES

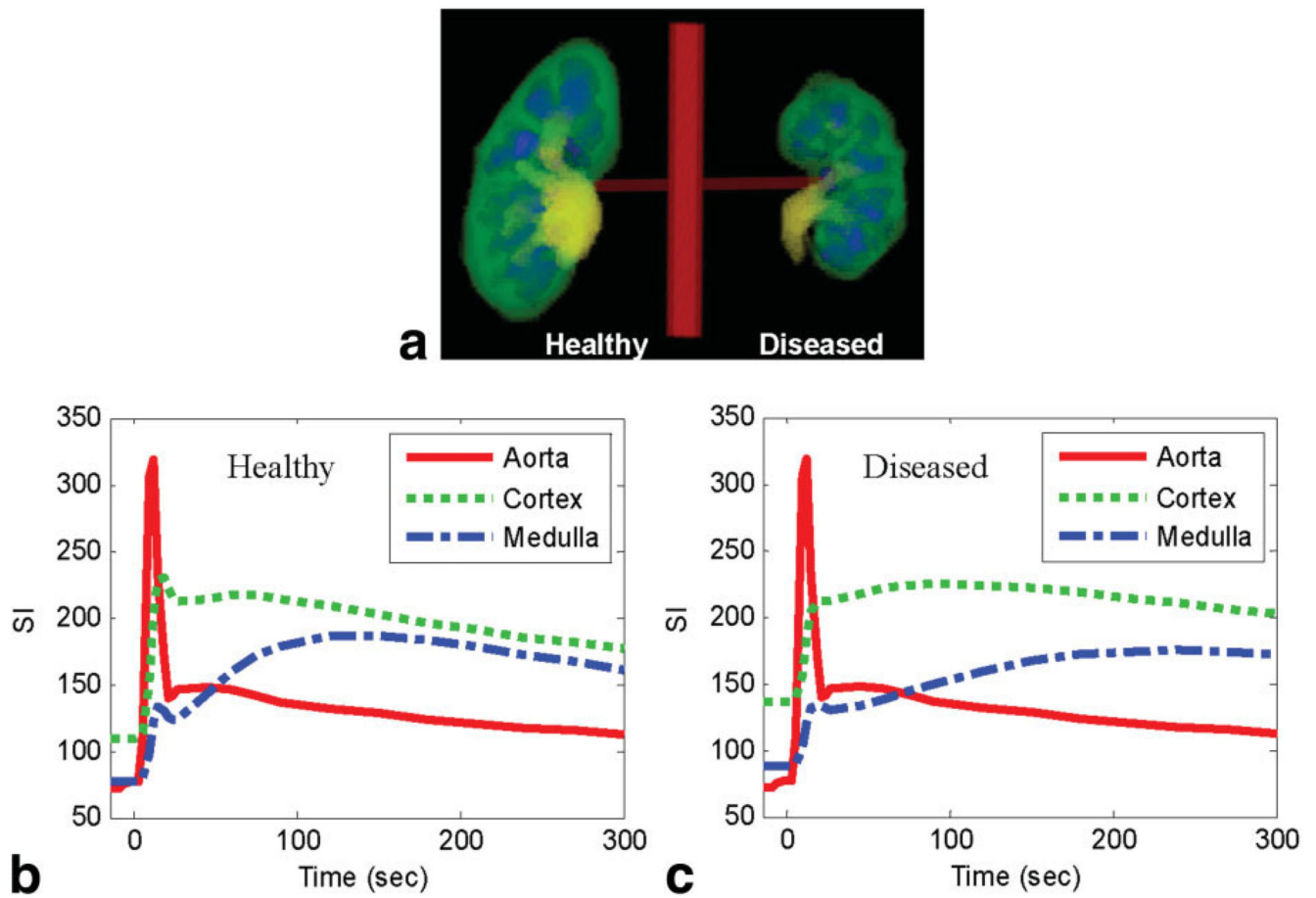
1. Gribbestad, IS.; Gjesdal, KI.; Nilsen, G.; Lundgren, S.; Hjelstuen, MHB.; Jackson, A. An introduction to dynamic contrast-enhanced MRI in oncology. In: Jackson, A.; Buckley, DL.; Parker, GJM., editors. Dynamic contrast-enhanced magnetic resonance imaging in oncology. New York: Springer; 2005. p. 3-22.
2. Swan JS, Carroll TJ, Kennell TW, Heisey DM, Korosec FR, Frayne R, Mistretta CA, Grist TM. Time-resolved three-dimensional contrast-enhanced MR angiography of the peripheral vessels. *Radiology* 2002;225:43–52. [PubMed: 12354982]
3. Michaely HJ, Schoenberg SO, Oesingmann N, Ittrich C, Buhlig C, Friedrich D, Struwe A, Rieger J, Reininger C, Samtleben W, Weiss M, Reiser MF. Renal artery stenosis: functional assessment with dynamic MR perfusion measurements—feasibility study. *Radiology* 2006;238:586–596. [PubMed: 16436819]
4. Lee VS, Rusinek H, Noz ME, Lee P, Raghavan M, Kramer EL. Dynamic three-dimensional MR renography for the measurement of single kidney function: initial experience. *Radiology* 2003;227:289–294. [PubMed: 12615998]
5. Van Vaals JJ, Brummer ME, Dixon WT, Tuithof JJ, Engels J, Nelson RC, Gerety BM, Chezmar JL, denBoer JA. “Keyhole” method for accelerating imaging of contrast agent uptake. *J Magn Reson Imaging* 1993;3:671–675. [PubMed: 8347963]
6. Doyle M, Walsh EG, Blackwell GG, Pohost GM. Block regional interpolation scheme for k-space (BRISK): a rapid cardiac imaging technique. *Magn Reson Med* 1995;33:163–170. [PubMed: 7707905]
7. Parrish T, Hu X. Continuous update with random encoding (CURE): a new strategy for dynamic imaging. *Magn Reson Med* 1995;33:326–335. [PubMed: 7760701]
8. Korosec FR, Frayne R, Grist TM, Mistretta CA. Time-resolved contrast-enhanced 3D MR angiography. *Magn Reson Med* 1996;36:345–351. [PubMed: 8875403]
9. Maki J, Prince M, Lundy F, Chenevert T. The effects of time varying intravenous signal intensity and k-space acquisition order on three-dimensional MR angiography image quality. *J Magn Reson Imaging* 1996;6:642–651. [PubMed: 8835958]
10. Tsao J, Boesiger P, Pruessmann KP. k-t BLAST and k-t SENSE: Dynamic MRI with high frame rate exploiting spatiotemporal correlations. *Magn Reson Med* 2003;50:1031–1042. [PubMed: 14587014]
11. Henderson E, Rutt BK, Lee TY. Temporal sampling requirements for the tracer kinetics modeling of breast disease. *Magn Reson Imaging* 1998;16:1057–1073. [PubMed: 9839990]
12. Lee VS, Rusinek H, Bokacheva L, Huang A, Oesingmann N, Chen Q, Kaur M, Prince K, Song T, Kramer E, Leonard E. Renal function measurements from MR renography and a simplified



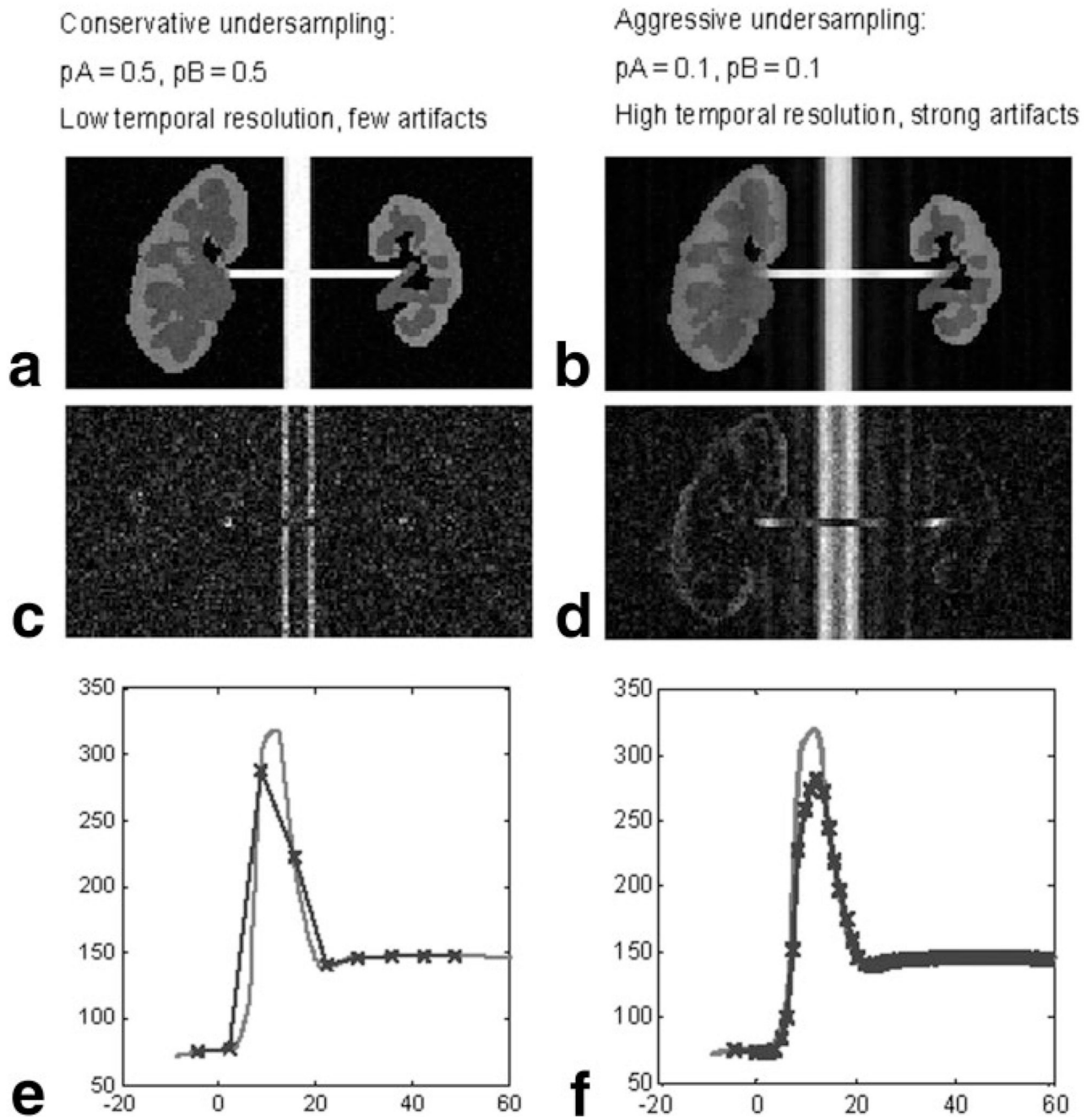
- multicompartmental model. *Am J Physiol Renal Physiol* 2007;292:F1548–F1559. [PubMed: 17213464]
13. Vogt, FM.; Eggebrecht, H.; Laub, G.; Kroeker, R.; Schmidt, M.; Barkhausen, J.; Ladd, SC. *Proc ISMRM*. Berlin: 2007. High spatial and temporal resolution MRA (TWIST) in acute aortic dissection; p. 92
  14. Lim RP, Shapiro M, Wang EY, Law M, Babb JS, Rueff LE, Jacob JS, Kim S, Carson RH, Mulholland TP, Laub G, Hecht EM. 3D time-resolved MR angiography (MRA) of the carotid arteries with time-resolved imaging with stochastic trajectories: comparison with 3D contrast-enhanced bolus-chase MRA and 3D time-of-flight MRA. *AJNR Am J Neuroradiol* 2008;29:1847–1854. [PubMed: 18768727]
  15. Rusinek H, Boykov Y, Kaur M, Wong S, Bokacheva L, Sajous JB, Huang AJ, Heller S, Lee VS. Performance of an automated segmentation algorithm for 3D MR renography. *Magn Reson Med* 2007;57:1159–1167. [PubMed: 17534915]
  16. Bokacheva L, Rusinek H, Chen Q, Oesingmann N, Prince C, Kaur M, Kramer E, Lee VS. Quantitative determination of Gd-DTPA concentration in T1-weighted MR renography studies. *Magn Reson Med* 2007;57:1012–1018. [PubMed: 17534906]
  17. Gauvrita J-Y, Lawb M, Xuc J, Carsonb R, Sunenshineb P, Chen Q. Time-resolved MR angiography: optimal parallel imaging method. *AJNR Am J Neuroradiol* 2007;28:835–838. [PubMed: 17494652]
  18. Mende KA, Froehlich JM, von Weyarn C, Hoogeveen R, Kistler T, Zollikofer CL, Wentz KU. Time-resolved, high-resolution contrast-enhanced MR angiography of dialysis shunts using the CENTRA keyhole technique with parallel imaging. *J Magn Reson Imaging* 2007;25:832–840. [PubMed: 17345633]
  19. Frydrychowicz A, Bley TA, Winterer JT, Harloff A, Langer M, Hennig J, Markl M. Accelerated time-resolved 3D contrast-enhanced MR angiography at 3T: clinical experience in 31 patients. *Magn Reson Mater Phys Biol Med* 2006;19:187–195.
  20. Sadowski EA, Bennett LK, Chan MR, Wentland AL, Garrett AL, Garrett RW, Djamali A. Nephrogenic systemic fibrosis: risk factors and incidence estimation. *Radiology* 2007;243:148–157. [PubMed: 17267695]



**FIG. 1.** TWIST acquisition. **a:** The 3D  $k$ -space with readout direction  $K_x$  and phase-encoding (PE) plane  $K_y-K_z$  is divided into low-frequency region A with radial distance in PE plane  $k_r < K_c$  and high-frequency region B with  $k_r \geq K_c$ . **b:** In  $K_y-K_z$  PE plane (shown here with  $15 \times 15$  points), region A ( $p_A = 0.5$ , is sampled fully every time. Region B is divided into  $n = 3$  trajectories B<sub>1</sub>, B<sub>2</sub>, and B<sub>3</sub>  $\approx 0.33$ ). **c:** Sampling proceeds first from the edge of A ( $k_r = K_c$ ) toward lower  $k_r$  and then back to  $K_c$ . In B, points are first sampled as  $k_r$  increases and then in reverse direction. **d:** In TWIST dynamic series of 3D images, full  $k$ -space is acquired only during the first acquisition ( $t = t_1$  in this example). Thereafter, for each image all points in A and only one of the B trajectories are sampled. Missing portions of B are copied from adjacent frames illustrated in a forward data-sharing scheme.



**FIG. 2.** Simulated 3D renal phantom. **a:** Volume rendering of the anatomical structure of the aorta and renal arteries (red), cortex (green), medulla (blue), collecting system (yellow). A healthy, normal-sized right kidney and a diseased, atrophic left kidney with thin cortex are simulated. SI versus time curves in **(b)** healthy and **(c)** diseased kidney were generated using a three-compartment renal model.

**FIG. 3.**

Top row: TWIST images of renal phantom at time  $t = 9$  sec after the beginning of acquisition for conservative undersampling  $p_A = 0.5$ ,  $p_B = 0.5$  (**a**) and aggressive undersampling  $p_A = 0.1$ ,  $p_B = 0.1$  (**b**). Middle row: Subtraction images showing the difference between acquired and ground truth images. Conservative undersampling causes few artifacts (**c**), while aggressive undersampling leads to strong ringing artifacts (**d**). Bottom row: TWIST-sampled aortic SI curves (line with  $\times$  symbols) compared with the ideal aortic curves (solid line without symbols) during the first minute of the acquisition. Moderate undersampling (**e**) results in lower temporal resolution, while high undersampling leads to high temporal resolution (**f**). Note that

even with high temporal resolution in **(f)** the aortic peak is underestimated because of data sharing with adjacent images where aortic signal is lower.

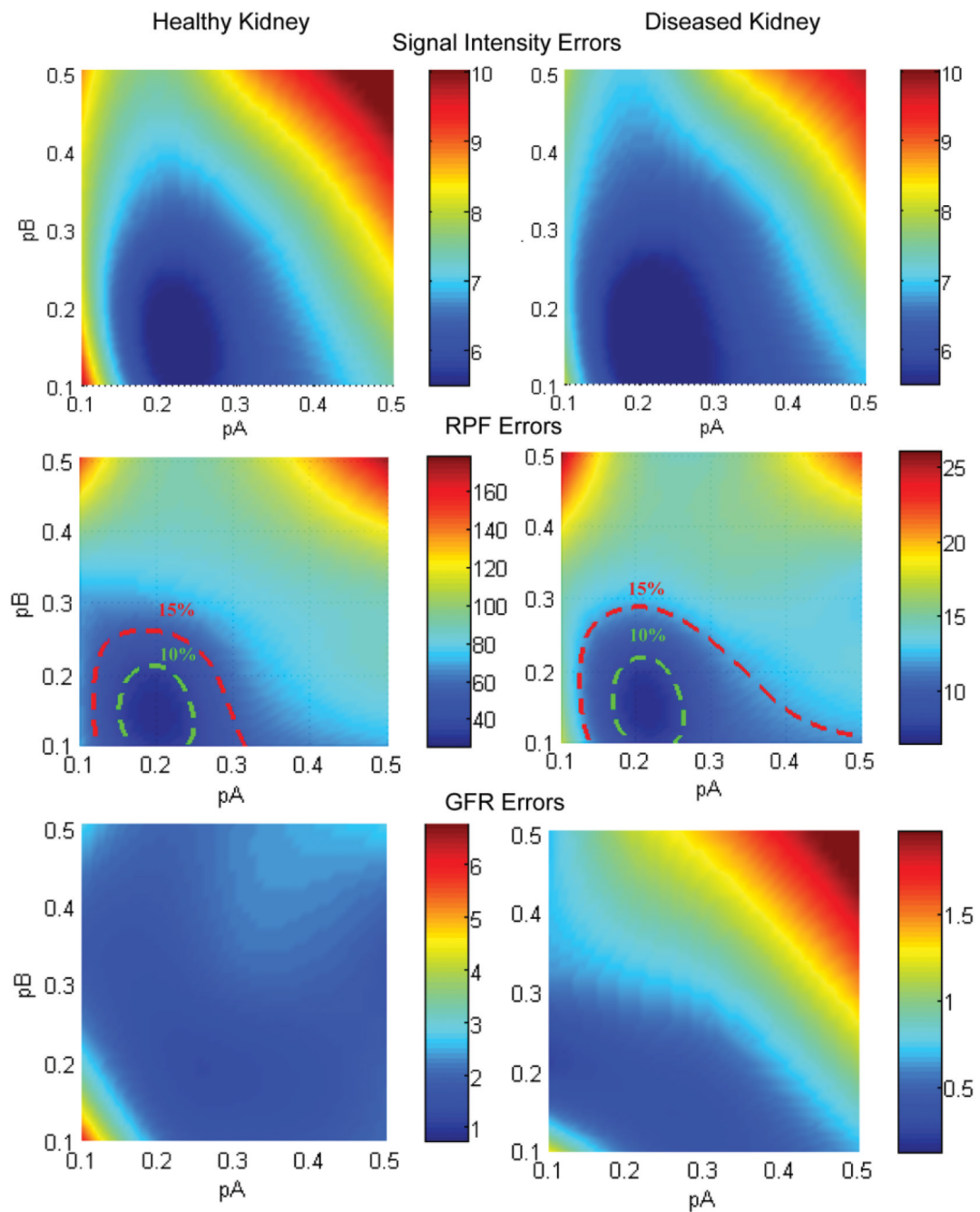


**FIG. 4.**

Errors due to TWIST undersampling as a function of parameters  $pA$  and  $pB$  for healthy (left column) and diseased (right column) kidneys. Top row: Cumulative (aortic, cortical, and medullary) SI errors show a minimum of 5% at approximately  $pA \approx 0.20$  and  $pB \approx 0.20$ . Middle row: Absolute RPF errors (in mL/min). The iso-contours indicate areas of relative RPF errors below 10% and 15%, at around  $pA \approx 0.20$  and  $pB \approx 0.20$  (reference RPF values are 346 mL/min and 78 mL/min for healthy and diseased kidney, respectively). Bottom row: Absolute GFR errors (in mL/min). Relative GFR errors are less than 10% of the reference values (reference GFR is 77 mL/min for the healthy kidney and 17 mL/min for the diseased kidney).



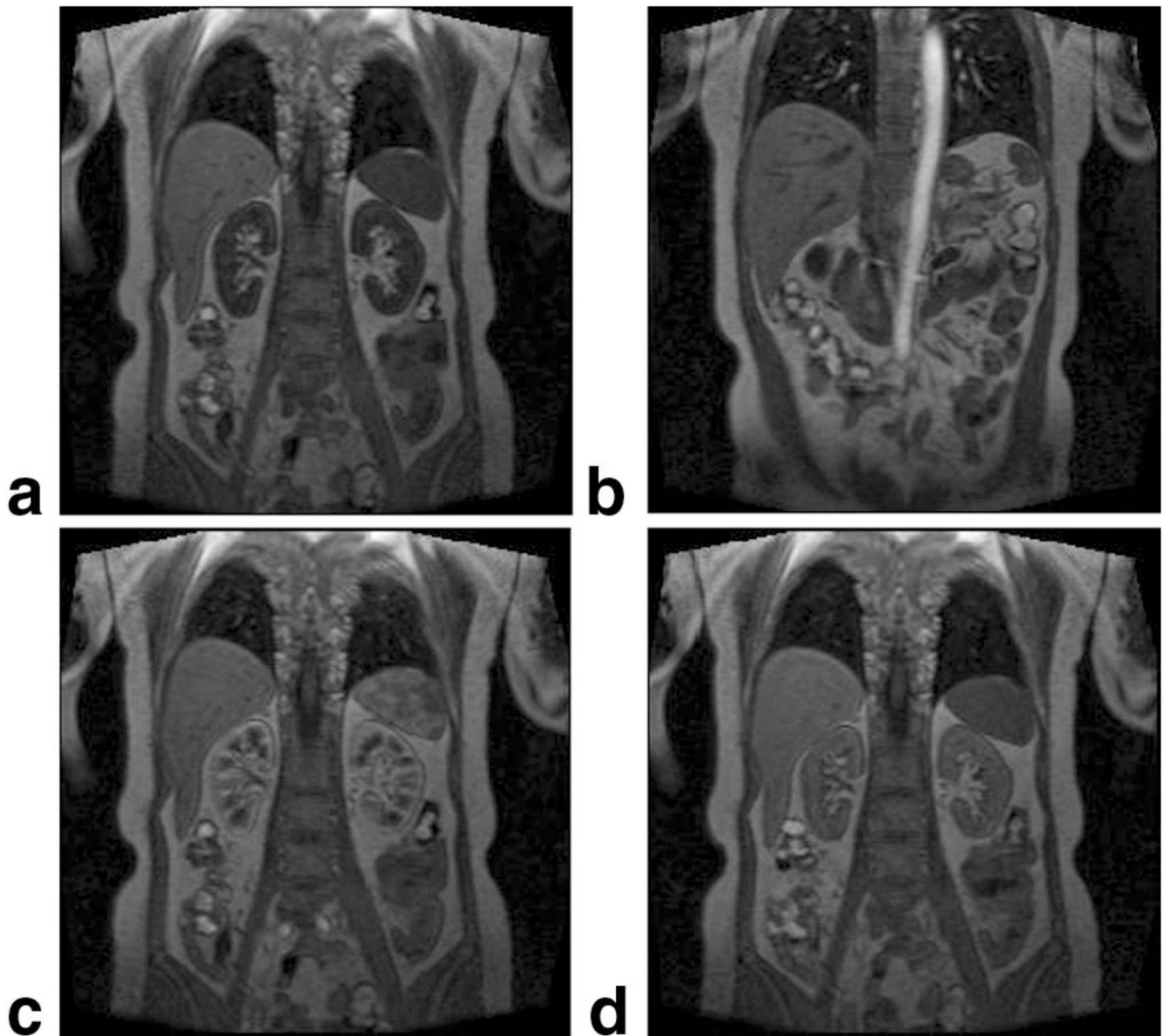


**FIG. 5.** TWIST MRR images of a 48-year-old female patient acquired using 3D GRE sequence with the following parameters: TR/TE/FA = 2.61/1.07/12°, bandwidth 650 Hz, FOV 425 mm × 425 mm × 100 mm, acquisition matrix 256 × 161 × 26, interpolated voxel 1.7 × 1.7 × 2.5 mm<sup>3</sup>; TWIST acquisition time 2.4 sec; pA = 0.2 and pB = 0.2. Images were acquired after the injection of 2 mL of Gd-DTPA at (a) t = 0 sec, (b) 19.3 sec (maximal aortic enhancement), (c) 24.1 sec (maximal cortical enhancement), (d) 70.1 sec (renal parenchymal enhancement).